ARTICLE

Three-dimensional Two-phase CFD Simulation of Alkaline Electrolyzers

Ling-Yu Gao [a], Lin Yang [a], Chen-Hui Wang [a], Gui-Xuan Shan [a], Xin-Yi Huo [a], Meng-Fei Zhang [a], Wei Li [a,b], Jin-Li Zhang [a,b,*]

[a] School of Chemical Engineering and Technology, Tianjin University, Tianjin 300072, PR China
[b] Haihe Laboratory of Sustainable Chemical Transformations, Tianjin 300192, PR China

Abstract

The structural and operation parameters of the electrolyzer play important roles in the efficiency of alkaline water electrolysis. In this article, a three-dimensional numerical model coupled with the electric field and the Euler-Eulerian k-ϵ turbulence flow field was first established to simulate accurately the performance of alkaline electrolyzers, based on a compact assembly structure of the industrial alkaline water electrolyzers, especially at current densities higher than 5000 $A \cdot m^{-2}$. The simulation results are compared with the experimental data to verify the accuracy of the model. Suitable operating conditions for concentration, flow rate and the optimal design method of the flow channel structure are obtained from the feedback of the electric and flow fields characteristics inside the electrolyzers. Properly increasing the electrolyte concentration and flow rate facilitates the reduction of cell voltage. The optimum concentration and flow rate of potassium hydroxide aqueous solution are evaluated to be 6.0−8.0 $mol \cdot L^{-1}$ and 30.0−45.0 $mL \cdot min^{-1}$, respectively. With the increase of the gap between electrode and membrane, the ohmic overpotential increases significantly. The triangular arrangement of conductive columns on the bipolar plate and the increase of the channel height are beneficial to improve the distribution uniformity of the fluid, while the channel height and the arrangement of the conductive columns have little effect on the voltage. Appropriately increasing the spacing between the conductive columns facilitates to reduce the voltage. Multiple outlets and inlets structure is conducive to produce a more uniform fluid distribution. The channel height has little effect on the multiple outlets and inlets electrolyzer. The multiple outlets and inlets electrolyzer G-2.5-T-0-5-3 with wide spacing of conductive columns combined with high flow rate not only can reduce the cell voltage, but also enhance the normal flow rate of the electrolyte on the electrode surface, allowing the best performance of the electrolyzer. This work provides useful guidance on the scale-up design and optimization of highly efficient electrolyzer for alkaline water electrolysis.

Keywords: Alkaline electrolyzer; Three-dimensional; Two-phase; Flow channel; Current density distribution

1. Introduction

Alkaline water electrolysis (AWE) is currently considered as the most promising industrial process to produce clean and sustainable "Green hydrogen" with the advantage of low cost, comparing with the proton exchange membrane water electrolysis (PEM) and solid oxide water electrolysis (SOE) [1−4]. The structural and operational parameters of the electrolyzer play important roles in the performance of AWE, however, it is hard to characterize certain features of the electrolyzer, such as the gas release behavior inside the electrodes, the distribution of current density, the evolution of overpotential, and so on. Such unclear features are fundamental to scale-up design of highly efficient electrolyzer for AWE.

Computational fluid dynamics (CFD) calculations have been used recently to study the complex multiphase flow and reaction behavior in electrolyzers [5,6], the mass transfer and the thermal properties during the electrochemical process, etc [7−10]. For instance, Han et al. [11] and Abdin et al. [12] revealed the influence of mass transfer

Received 8 July 2022; Received in revised form 15 February 2023; Accepted 21 February 2023
Available online 27 February 2023

* Corresponding author, Jin-Li Zhang, Tel: (86-22)27403389, E-mail address: zhangjinli@tju.edu.cn.

https://doi.org/10.13208/j.electrochem.2207081

properties on diffusion overpotentials and evaluated the effects of gas cross-permeation. Alexiadis [13] and De Groot [14] found out that bubbles generated from the reaction could cover the effective surface of the electrode, resulting in a significant increase in the activation overpotential and ohmic overpotential. These results suggested the significant effect of the generated bubbles on the *I-V* characteristic curve and hydrodynamic characteristics in an electrolyzer.

To study the bubble influence on the electric field, some numerical simulations introduced the bubble effect as a correlation function of the current density. Rodriguez et al. [15] established a two-dimensional (2D) CFD model of an alkaline electrolyzer by coupling the electric field and flow field, and showed that the generated gas produced a "curtain profile" in the electrode. In addition, some models have been established to correlate the bubble growth rate and coverage with temperature, diffusion coefficient and current density [16,17]. Shen et al. [18] analyzed the bubble behavior in the milli-scale serpentine flow channel and found out that the low-velocity region of the round-corner flow channel was smaller than that of the square-corner one, which can reduce the stagnation time of bubbles. Based on the CFD calculation using Euler-Euler laminar flow, Ju et al. [19] concluded that the nucleation of bubbles occurred in low electrolyte flow rates or large electrolyzers, which increased ohmic and activation overpotentials. However, CFD calculations still needs to be improved, so as to simulate the electrolyzer accurately.

Most of these numerical simulations made assumption of a constant gas production rate over the electrode surface, which is beneficial to achieve the convergence results. However, in the real AWE process the rate of gas generation is proportional to the volume current density, which is not uniform due to the gas coverage, according to Faraday's law. Moreover, recent work disclosed that the presence of air bubbles caused turbulence in the electrolyzer [20,21]. Whereas most of the simulations assumed the laminar flow in the electrolyzer, ignoring that the turbulence would result in the underestimation of the AWE performance. Thus, aiming at accurately simulating the electrolyzer, it is urgent to develop a two-phase turbulence model to describe the generation of gas in AWE, considering the volume current density associated with the current distribution.

On the other hand, the channel construction of industrial alkaline electrolyzers is fundamental to affect the turbulent flow patterns during AWE process. Dunnill [22] and Haverkort [23] claimed that the zero-gap electrolyzer would allow for a lower ohmic resistance, as well as reduce the effect of the gas bubbles on the performance of electrolyzer. However, no report has been found so far on the study of physical processes in three-dimensional (3D) zero-gap alkaline water electrolyzers.

In this article, a 3D numerical model coupled with the electric field and the Euler-Eulerian k-ϵ turbulence flow field is established to simulate accurately the performance of alkaline electrolyzers, based on a compact assembly structure of the industrial alkaline water electrolyzers. The dual effect between

Nomenclature

AWE	Alkaline water electrolysis
c	Continuous phase
C_{KOH}	KOH aqueous solution concentration [mol·L^{-1}]
C_ϵ	Constants of the turbulence model
d	Dispersed phase
D_{md}	Turbulent dispersion coefficient
E_0	Thermodynamic equilibrium potential [V]
F	Faraday's constant 96,500 [C·mol^{-1}]
F_m	Volume force [N·m^{-2}]
g	Gravitational acceleration 9.81 [m·s^{-2}]
HER	Hydrogen evolution reaction
h_ch	The channel height [mm]
h_w	The gap between electrode and electrolyte membrane [mm]
h_y	Distance between the electrode section and electrolyte membrane surface [mm]
i	Current density [A·m^{-2}]
I	Unit tensor
i_0	Exchange current density [A·m^{-2}]
i_v	Reaction current density [A·m^{-3}]
M_{H2}	The relative molecular mass of H_2 2 [g·mol^{-1}]
M_{O2}	The relative molecular mass of O_2 32 [g·mol^{-1}]
OER	Oxygen evolution reaction
p	Pressure scalar [Pa]
PEM	Proton exchange membrane
phid	Gas volume fraction
Q_{in}	KOH aqueous solution inlet flow rate [mL·min^{-1}]
R	Ratio of KOH aqueous solution inlet flow to electrode area [mL·min^{-1}]
SOE	Solid oxide water electrolysis
u	Velocity vector [m·s^{-1}]
U_{cell}	Cell voltage [V]
u_m	Mixture velocity [m·s^{-1}]
u_y	Normal velocity of electrode surface [m·s^{-1}]
U_{rev}	Reversible voltage [V]
w_ch	The spacing of channel conductive columns[mm]
α	Transfer coefficient
η	Overpotential [V]
μ_T	Turbulent kinematic viscosity [m^2·s^{-1}]
ρ	Density [kg·m^{-3}]
σ_0	Electrolyte conductivity without the influence of gas [S·m^{-1}]
σ_e	Electrolyte conductivity [S·m^{-1}]
σ_T	Turbulence model parameters
τ	Viscous shear stress [N·m^{-2}]
Φ_g	Gas volume fraction

the bubble flow and electrochemical process is considered to accurately estimate the gas release behavior and hydrodynamic characteristics of AWE electrolyzer with different structures, especially at current densities higher than 5000 $A \cdot m^{-2}$. The CFD calculation results are compared with the experimental data to verify the accuracy of the model. By predicting the stability time under different operating conditions, it provides a basis for designing computing time nodes for future simulation research. Suitable operating conditions for concentration, flow rate and the optimal design method of the flow channel structure are obtained from the feedback of the electric and flow fields characteristics inside the electrolyzers.

2. Methodology

2.1. Mathematical models of the electrolyzer

2.1.1. Electrochemical model

Eqs. (1) and (2) show the half-cell reactions and the corresponding electrode potentials at 298.15 K and standard atmospheric pressure [24].

$$\text{Cathode: } 2H_2O + 2e^- \rightarrow H_2 + 2OH^-$$
$$E^0 = -0.8280\ \text{V} \quad (1)$$

$$\text{Anode: } 2OH^- \rightarrow 0.5O_2 + H_2O + 2e^-$$
$$E^0 = +0.4011\ \text{V} \quad (2)$$

In the alkaline water electrolyzer model, KOH aqueous solution is adopted as the electrolyte, of which OH^- group would be transported through the porous membrane. The porosities of the porous electrode and membrane are set as 0.85 and 0.56, respectively, and the conductivity of 30 wt% KOH aqueous solution is 138 $S \cdot m^{-1}$ at 80 °C [15,25]. The equilibrium potential of the electrolysis is calculated by the Nernst equation. The potential difference may deviate from its equilibrium value due to the additional impedance caused by the limited rate of the electrolytic reaction. The difference between the actual potential and the equilibrium potential is the activation overpotential η_{act} (V). Due to the existence of overpotential, there is a difference between the current conservation equation and the potential equation at the electrode-electrolyte interface as shown in Eqs. (3)–(5).

Electrode	$i_s = -\sigma_s \nabla \phi_s \nabla \cdot i_s = Q_S$	(3)
Electrolyte	$i_l = -\sigma_l \nabla \phi_l \nabla \cdot i_l = Q_l$	(4)
Interface	$\eta_{act} = \phi_s - \phi_l - E_{eq}$	(5)

where i_s ($A \cdot m^{-2}$) and i_l ($A \cdot m^{-2}$) represent the current density vectors, σ ($S \cdot m^{-1}$) represents the electrical conductivity, and φ (V) represents the potential between the metal conductor and electrolyte. The subscripts s and l represent the electrode and the electrolyte, respectively.

Activation overpotential is an irreversible voltage loss induced by the oxygen evolution and hydrogen evolution reactions occurring on the anode and cathode sides, respectively. The Butler-Volmer equation [15] is used to estimate the activation overpotentials η_{act} for the cathode and anode electrodes in Eq. (6). According to Eq. (7), the sum of the reaction currents of all electrodes is used as the current density condition on the boundary between the electrode and the electrolyte domain. The additional capacitive current density i_{dl} ($A \cdot m^{-2}$) is generated by the charging and discharging processes of the electric double layer.

$$\eta_{act} = 2.3 \cdot \frac{RT}{\alpha F} \cdot \log\left(\frac{i}{i_0}\right) \quad (6)$$

$$-i_s \cdot \mathbf{n} = i_l \cdot \mathbf{n} = \frac{\partial(\phi_s - \phi_l)}{\partial t} \cdot C_{dl} = \frac{\partial \eta}{\partial t} \cdot C_{dl} \quad (7)$$

where i ($A \cdot m^{-2}$) is the current density, R ($J \cdot (mol \cdot k)^{-1}$) is the gas constant, and α is the charge transfer coefficient, F ($C \cdot mol^{-1}$) is Faraday's constant, η (V) is the overpotential, and C_{dl} ($F \cdot m^{-2}$) is the differential capacity per unit area. The exchange current densities i_{01} ($A \cdot m^{-2}$) of the hydrogen evolution reaction (HER) and i_{02} ($A \cdot m^{-2}$) of oxygen evolution reaction (OER), and the transfer coefficient α of porous nickel electrodes in an alkaline solution (30 wt% KOH) are summarized in Table 1.

According to the Bruggeman equation [29], the electrolyte conductivity σ_e ($S \cdot m^{-1}$) is related to the gas volume fraction Φ_g in Eq. (8). The conductivity under the influence of gas is calculated according to the volume fraction of gas in the Euler-Euler model. σ_0 ($S \cdot m^{-1}$) is the conductivity of the electrolyte without the influence of the gas.

Table 1. Electrode kinetic parameters.

Description	Value
Exchange current density at nickel foam negative electrode at 80 °C, i_{01}^{ref}	23.4 $A \cdot m^{-2}$ [26]
Exchange current density at nickel foam positive electrode at 70 °C, i_{02}^{ref}	9.3 $A \cdot m^{-2}$ [27]
Transfer coefficient at nickel foam negative electrode, α_1	0.5 [28]
Transfer coefficient at nickel foam positive electrode, α_2	0.5 [28]

$$\sigma_e = \sigma_0 \cdot \left(1 - \Phi_g\right)^{1.5} \tag{8}$$

The actual cell voltage U (V) is always higher than the irreversible voltage due to irreversibility and overpotential [15]. Therefore, the actual voltage is defined as the sum of the reversible voltage U_{rev} (V) and the overpotential η (V) as shown in Eq. (9).

$$U = U_{rev} + \sum \eta \tag{9}$$

where the $\Sigma\eta$ (V) term is the sum of the activation and ohmic overpotentials.

2.1.2. Two-phase Euler-Euler k-ϵ turbulence model

The Euler-Euler model defines the momentum equations and continuity equations for each phase, and the k-ϵ model is used for turbulent closure. With this method, two-phase flow thorough the porous electrode is described in terms of the mass-averaged mixture velocity and mass flux. Under the above-mentioned assumptions, the proposed transient isothermal model for porous structures is governed by the following conservation equations [15,19].

Momentum conservation equations can be obtained by summing the individual momentum equations of the two phases as follows.

$$\rho_c(u_c \cdot \nabla)u_c = \nabla \cdot \left[-p\mathbf{I} + \tau_c\right] + \rho_c \mathbf{g} + \frac{F_{m,c}}{\phi_c} + F_c + \frac{m_{dc}}{\phi_c}(\mathbf{u}_{int} - \mathbf{u}_c) \tag{10}$$

$$\rho_d(u_d \cdot \nabla)u_d = \nabla \cdot \left[-p\mathbf{I} + \tau_d\right] - \frac{\nabla p_s}{\phi_d} + \rho_d \mathbf{g} + \frac{F_{m,d}}{\phi_d} + F_d - \frac{m_{dc}}{\phi_d}(u_{int} - u_d) \tag{11}$$

where ρ (kg·m^{-3}), u (m·s^{-1}), p (pa), I, F (N·m^{-2}), φ, and τ (N·m^{-2}) are the density, velocity vector, pressure scalar, unit tensor, volume force, fraction and the viscous shear stress of each phase, respectively. The subscripts d and c represent the dispersed phase and continuous phase, respectively.

The continuity equations of the continuous phase and the dispersed phase are expressed in Eqs. (12) and (13).

$$\nabla \cdot (\phi_c u_c + \phi_d u_d) = m_{dc}\left(\frac{1}{\rho_c} - \frac{1}{\rho_d}\right), \phi_d = \text{phid}, \phi_c = 1 - \phi_d \tag{12}$$

$$\nabla \cdot (\phi_d u_d) - \nabla \cdot (D_{md} \nabla \phi_d) = \frac{m_{dc}}{\rho_d}, D_{md} = \frac{\mu_T}{\rho \sigma_T} \tag{13}$$

where phid, D_{md}, μ_T (m^2·s^{-1}), and σ_T are the gas volume fraction, turbulent dispersion coefficient, turbulent kinematic viscosity, and turbulence model parameters, respectively.

Different turbulence models are compared, and the k-ϵ model is used in this study because it can better predict the experimental results [30]. A wall function is used to have a good convergence rate and relatively low memory requirements. Two additional variables are solved in Eqs. 14–16: the turbulent kinetic energy k (m^2·s^{-2}) and the turbulent energy dissipation rate ϵ (m^2·s^{-3}).

$$\mu_T = \rho C_\mu \frac{k^2}{\epsilon} \tag{14}$$

$$\rho(u_m \cdot \nabla)k = \nabla \cdot \left[\left(\mu_m + \frac{\mu_T}{\sigma_k}\right)\nabla k\right] + P_k - \rho\epsilon \tag{15}$$

Table 2. Size parameters of electrolyzers in different geometric structures.

Structure name	h_ch (mm)	Arrangement of conductive columns	h_w (mm)	w_ch (mm)	Number of inlet/outlet
G-2.5-T-0-3-1	2.5	Triangular	0	3	1
G-2.5-T-0.05-3-1	2.5	Triangular	0.05	3	1
G-2.5-T-1-3-1	2.5	Triangular	1	3	1
G-2.5-T-2-3-1	2.5	Triangular	2	3	1
G-2.25-T-0-3-1	2.25	Triangular	0	3	1
G-3-T-0-3-1	3	Triangular	0	3	1
G-2.5-S-0-3-1	2.5	Square	0	3	1
G-2.5-T-0-3-3	2.5	Triangular	0	3	3
G-2.5-T-0-5-1	2.5	Triangular	0	5	1
G-2.5-S-0-5-1	2.5	Square	0	5	1
G-2.5-S-0-7-1	2.5	Square	0	7	1
G-2.25-T-0-3-3	2.25	Triangular	0	3	3
G-3-T-0-3-3	3	Triangular	0	3	3
G-2.5-T-0-5-3	2.5	Triangular	0	5	3
G-2.5-S-0-5-3	2.5	Square	0	5	3
G-2.5-S-0-7-3	2.5	Square	0	7	3

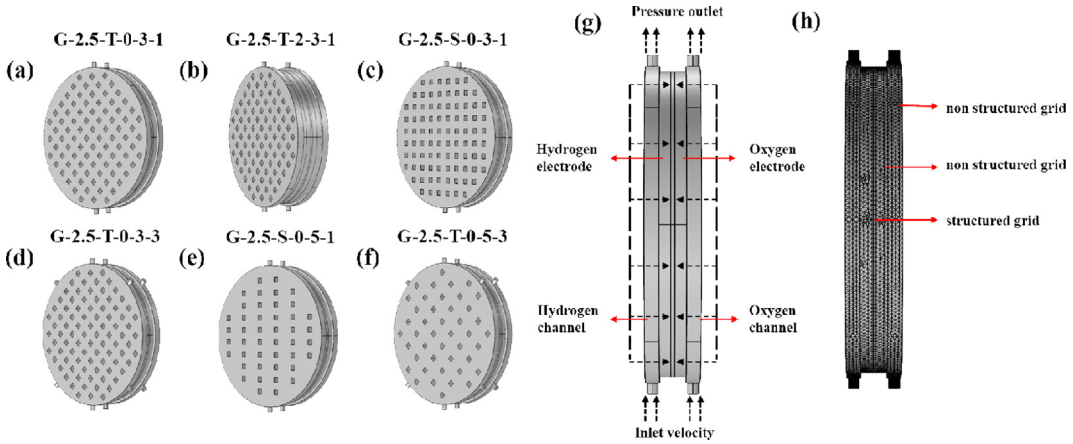

Fig. 1. (a–f) Representative geometric models of electrolyzers with different structures; (g) Boundary condition settings; (h) Meshing.

$$\rho(u_m \cdot \nabla)\epsilon = \nabla \cdot \left[\left(\mu_m + \frac{\mu_T}{\sigma_\epsilon}\right)\nabla\epsilon\right] + C_{\epsilon,1}\frac{\epsilon}{k}P_k - C_{\epsilon,2}\rho\frac{\epsilon^2}{k} \quad (16)$$

where u_m ($m \cdot s^{-1}$) is the mixture velocity, and $C_{\epsilon,1}$, $C_{\epsilon,2}$ are the constants of the turbulence model, which are 1.44 and 1.92, respectively [31].

The sources of H_2 and O_2 are defined according to Faraday's law [32], and calculated using Eq. (17).

$$m_{H_2} = \frac{M_{H_2}}{2 \cdot F} \cdot i_v \; m_{O_2} = \frac{M_{O_2}}{4 \cdot F} \cdot i_v \quad (17)$$

where i_v ($A \cdot m^{-3}$) is the volume current density. The coupling between electrochemistry and hydrodynamics is linked by the current density.

2.2. Geometry and boundary condition settings

To study the internal electric field and flow field distributions of the electrolyzer, sixteen types of alkaline electrolyzers are constructed with different geometric models, as listed in Table 2, and the representative geometric models are shown in Fig. 1(a–f). The nomenclature is named according to the order of geometric abbreviation: G-flow channel height, h_ch-arrangement of conductive columns-the gap between electrode and electrolyte membrane, h_w-the spacing of channel conductive columns, w_ch-the number of inlets and outlets (for example, G-2.5-T-0-3-1 represents an electrolyzer with a flow channel height of 2.5 mm, a triangular arrangement of conductive columns, a gap between electrode and membrane of 0 mm, a spacing between conductive columns of 3 mm and with only one inlet and outlet).

The electrolyzer model consists of an electrolyte membrane, cathode and anode, and flow channels on both sides. Fig. 1(g) shows the boundary condition settings. The electrolyte is 30 wt% KOH aqueous solution, and the electronically conducting phase is set to galvanostatic input and electrical ground. The mass sources of H_2 and O_2 are defined on the hydrogen-oxygen electrode according to Faraday's law. At the same time, considering the influence of electrolyte membrane resistance on electrolysis, the transport of hydroxide ions from the cathode to anode is designed on the electrolyte membrane. The boundary conditions use velocity inlet and pressure outlet. The continuous phase has velocity inlet, and

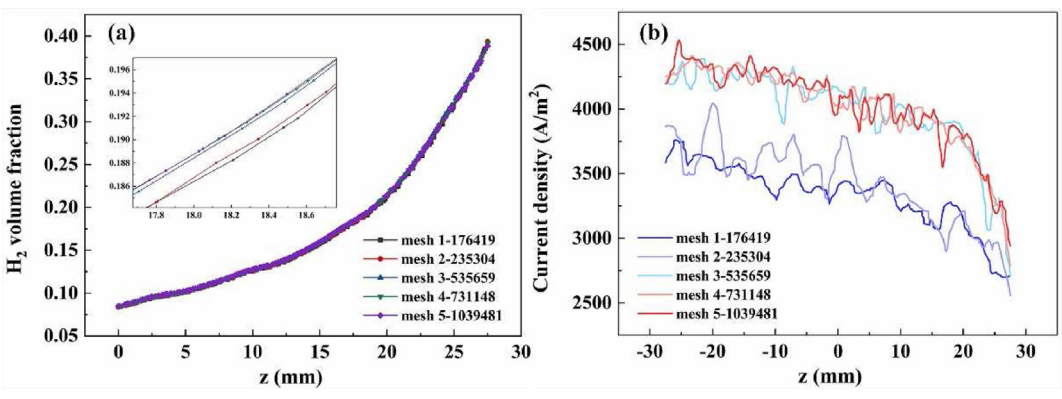

Fig. 2. Effects of different meshes on the solution results of (a) H_2 volume fraction; (b) current density distribution.

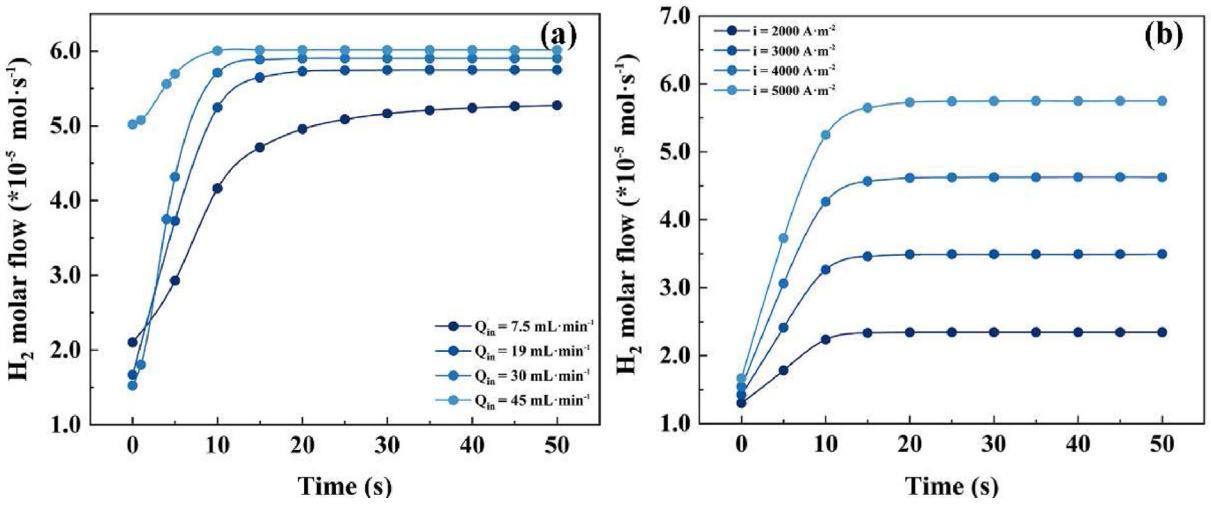

Fig. 3. Stability time results of different (a) KOH aqueous solution inlet flow rates; (b) current densities.

the dispersed phase boundary is selected without flux. All channel walls have no-slip boundary conditions except that all internal boundaries.

2.3. Solving method

The model is established and solved using the COMSOL V6.0; the stationary solver is used first to obtain a good initial value used to enhance the convergence of the model, and then the transient solver simulates the real state. The convergence condition of the solver is fixed as the relative error is less than 0.0001. The time step method is the backward difference formula (BDF) method and the storage time step size is set to 1 s. The parametric sweep method in the research extension is used to save computation time and memory space, and to improve convergence.

2.4. Mesh and dependency tests

Verification of mesh independence is the basis of finite element simulation analysis and the density of meshing affects the accuracy of the solution. The denser the mesh, the higher the accuracy of the mass transfer and momentum transfer analysis at the internal boundary of the electrolyzer, which in turn directly affects the accuracy of the gas volume fraction and current density results.

As shown in Fig. 1(h), based on establishing the geometric models of the circular and square electrolyzers, the flow channels and electrodes are divided by free tetrahedral meshes, and the electrolyte membrane part is divided by hexahedral meshes. Five different numbers of meshes (the mesh 1-176,419, mesh 2-235,304, mesh 3-535,659, mesh 4-731,148 and mesh 5-1039,481) are obtained. Fig. 2 shows that the number of meshes has a weak effect on the results for the H_2 volume fraction and a significant effect on the calculated results for the electrolyte current density. After the grid number reaches 731,148, the electrolyte current density distribution is no longer affected by the grid density, which indicates that the calculation accuracy can be guaranteed after the grid number reaches 731,148. Considering the length of calculation time and amount of cost, the final number of selected grids is 731,148, and the minimum cell quality is 0.1887.

2.5. Time dependency test

By monitoring the stability of the H_2 molar flow rate at the outlet, the stability time at different electrolyte flow rates Q_{in} = 7.5, 19, 30 and 45 $mL \cdot min^{-1}$ was tested. As shown in Fig. 3(a), the smaller the KOH aqueous solution flow rate, the longer the time required for stabilization. For example, under Q_{in} = 7.5 $mL \cdot min^{-1}$, the stabilization time of the electrolytic cell needs at least 45 s, while under Q_{in} = 45 $mL \cdot min^{-1}$, the required stabilization time is only 15 s. This is because the lower the flow rate, the slower the flow of fluid in the cell and the longer it takes for the gas and liquid to reach dynamic equilibrium.

As shown in Fig. 3(b), the larger the current density, the longer the required stabilization time. Therefore, the time required to reach stability when $i = 5000\ A \cdot m^{-2}$ can be used as a reference for setting the termination time. This also helps us to predict and judge the stability of the experiment in advance under certain conditions, and then record more accurate results.

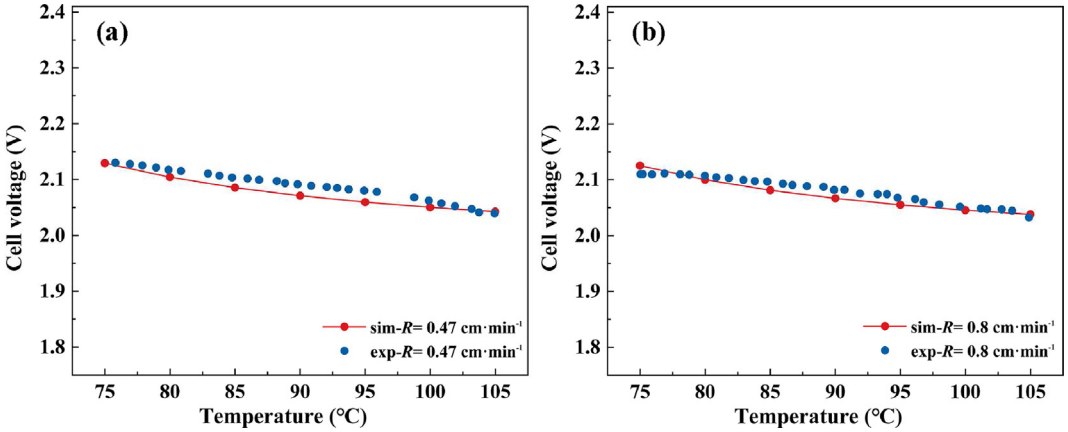

Fig. 4. Comparison between simulation results and experimental data at (a) R = 0.47 cm·min^{-1} and (b) R = 0.8 cm·min^{-1}.

2.6. Model validation

Fig. 4 indicates that when the ratios of inlet flow rate to electrode area R = 0.47 and 0.8 cm·min^{-1}, the maximum absolute deviations between the experimental data and simulation results for cell voltage are 0.875% and 1.02%, respectively. The CFD calculation results and the experimental data match well. Comparing the simulation results with Vogt's experiments [23] at different temperatures and current densities, the trend and magnitude of voltage change are in good agreement. This also fully demonstrates the accuracy of the coupling of the Euler-Euler k-ϵ turbulence model and the electric field for describing the macroscopic characteristics of the electrolyzer.

3. Results and discussion

3.1. Influence of gas on current density distribution

Electrolyzer G-2.5-T-0-3-1 is adopted to simulate the effect of operating parameters. Fig. 5 shows the current density distribution of the electrode at Q_{in} = 19 mL·min^{-1} and i = 5000 A·m^{-2}. Taking

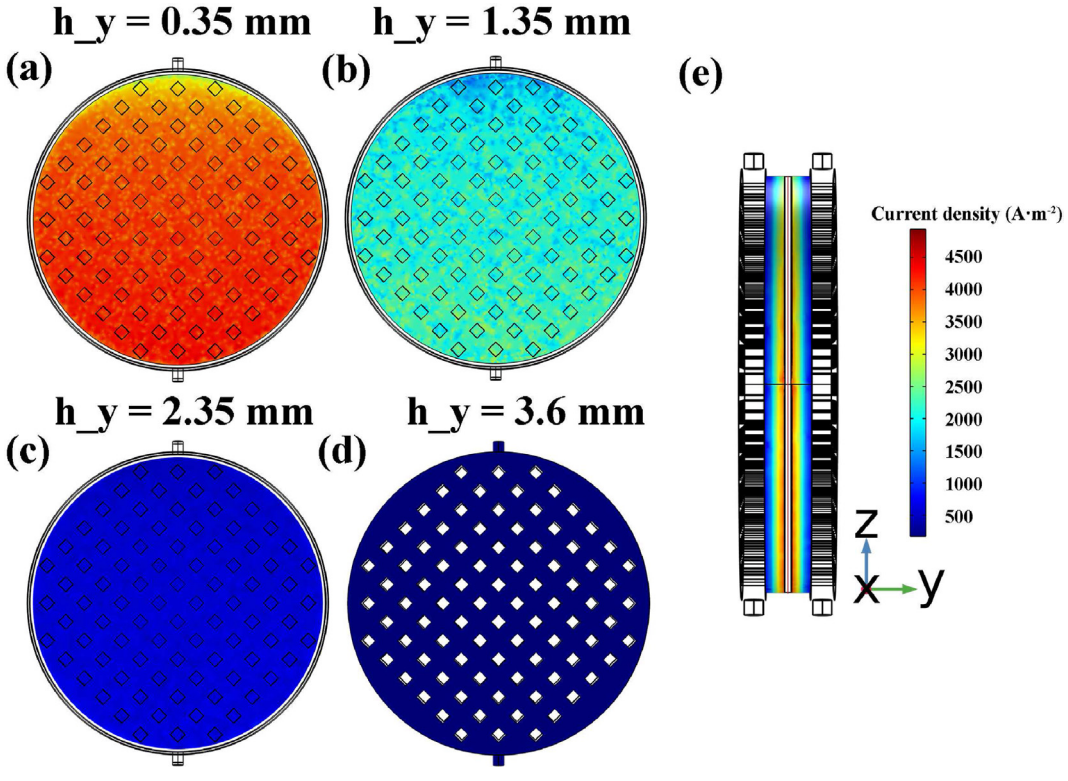

Fig. 5. (a–d) Front view of the distribution of current density at different electrode interfaces; (e) side view of current density distribution.

the center of the electrolyte membrane as the benchmark (shown by the red line in Fig. 5(e)), the changing trends of the electrolyte current density at the distances between the electrode section and electrolyte membrane surface h_y = 0.35 mm, 1.35 mm, 2.35 mm and 3.6 mm between the electrode section and the center of electrolyte membrane are analyzed. As shown in Fig. 5(a−d), in the *y*-direction, the closer to the electrolyte membrane, the larger the current density at the electrode surface. This is because both electronic and ionic conduction exists inside the cell. When the cathode or anode is close to the electrolyte membrane, the electrolyte current density is the total current density, and the closer it is to the bipolar plate interface, the more the electrolyte current density is converted into electrode current. So at the bipolar plate interface, the main is electrode current. Similarly, the closer to the electrolyte membrane, the greater the electrolyte current. Second, the electrolyte current density shows a decreasing trend along the exit direction of the *z*-axis. This is the result of gas accumulation at the outlet, resulting in a decrease in electrolyte current density. This corresponds to the side view of the electrolyte current density shown in Fig. 5(e). The gas fraction gradually increases toward longitudinally direction along the *z*-axis, so the current density has a clear downward trend near the flow channel, and the range of the small current density gradually widens.

3.2. *Influences of KOH aqueous solution concentration and flow rate on electrolyzer performance*

The effects of KOH aqueous solution on the performance and hydrodynamics of the electrolyzer are studied under different concentrations and flow rates Q_{in}. Fig. 6(a) shows that with the increase of KOH aqueous solution concentration, the cell voltage decreases first and then increases, reaching the lowest voltage of 2.0997 V at 8 mol·L^{-1}. This trend is because the increase of the concentration is beneficial to improve the electrolyte conductivity, while the concentration is increased to a certain level, the collision between the ions will be more intense, which may hinder the normal propagation of the ions, thereby increasing the ohmic overpotential. This is consistent with the trend of ohmic overpotential measured by De Dominici [6] at different KOH concentrations. Hence, the optimal KOH aqueous solution concentration operating ranges are 6−8 mol·L^{-1}.

An increase in the flow rate facilitates the removal of gas accumulated in the electrode, thus reducing the ohmic overpotential caused by the bubble effect; however, if the flow rate is too high, it also affects the ion transport and then the reaction rate. Therefore, it is significant to balance the effects of flow rate on both gas accumulation and reaction rate. Since the amount of reactants consumed is much less than the amount replenished, the reactants can also be replenished in time at high flow rates. To reduce power consumption, the effects of flow rate on gas accumulation and reaction rate are also ultimately reflected in whether an increase in flow rate favors a reduction in cell voltage.

As shown in Fig. 6(b), cell voltage decreases as the flow rate Q_{in} increases. The cell voltage for Q_{in} = 45 mL min^{-1} is 15 mV lower than that for Q_{in} = 7.5 mL·min^{-1}. Gas accumulation on the electrode covers the effective area of the electrode and destroys the double electron layer structure [33], which adversely affects the chemical reaction rate; the gas further hinders the inter-ion transfer and increases the ohmic overpotential. While, when Q_{in} was increased to 30 mL·min^{-1}, the cell voltage changed slightly [34]. This indicates that the effect of ion transport on the reaction rate becomes evident.

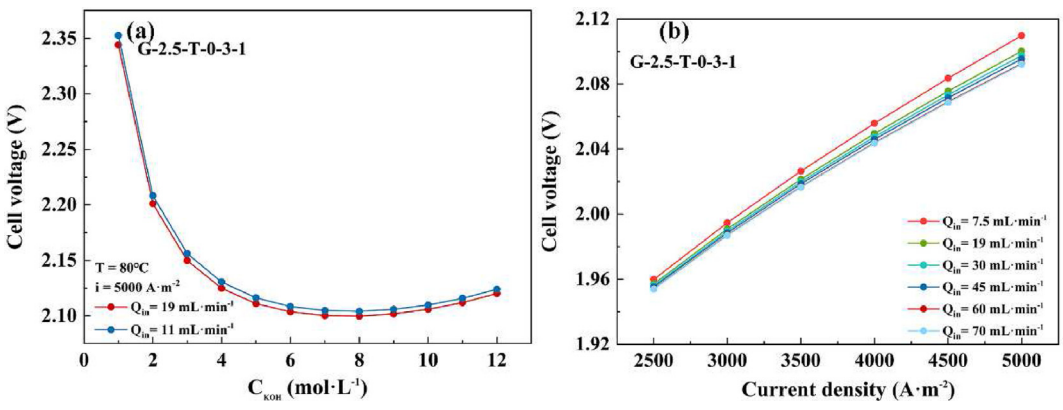

Fig. 6. The effects of (a) KOH aqueous solution concentration; (b) flow rate Q_{in} on cell voltage.

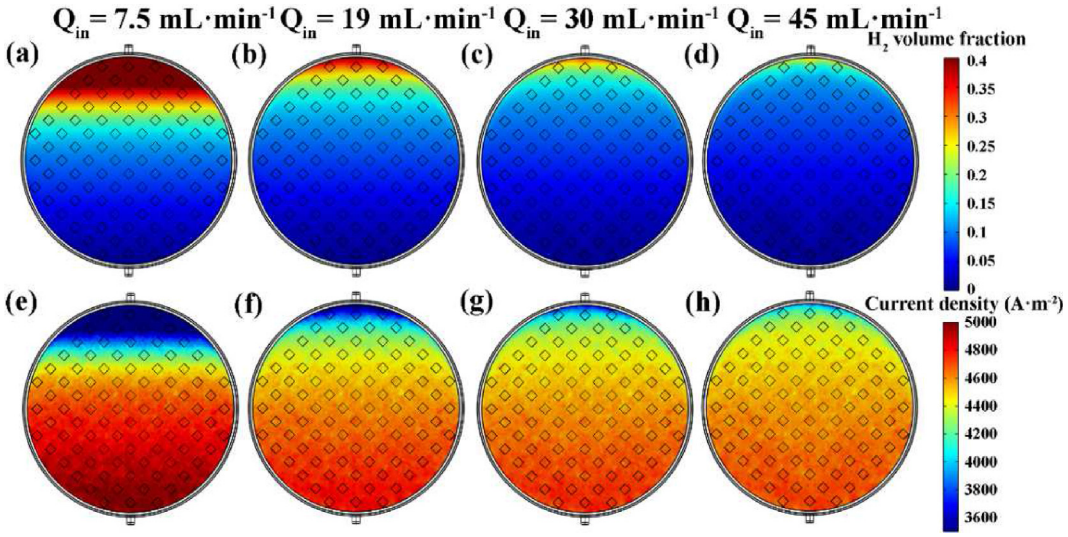

Fig. 7. The influences of flow rate Q_{in} on the distribution of (a—d) H_2; (e—f) the current density.

From the ultimate aim of reducing the cell voltage, the optimal range of flow rate should be between 30 and 45 mL·min^{-1} to balance the effects of flow rate on gas accumulation and reaction rate. Continue to increase the flow rate has little effect on the voltage, and this will increase the energy consumption of material transportation. And the flow rate 30—45 mL·min^{-1} converted to the circulation ratio

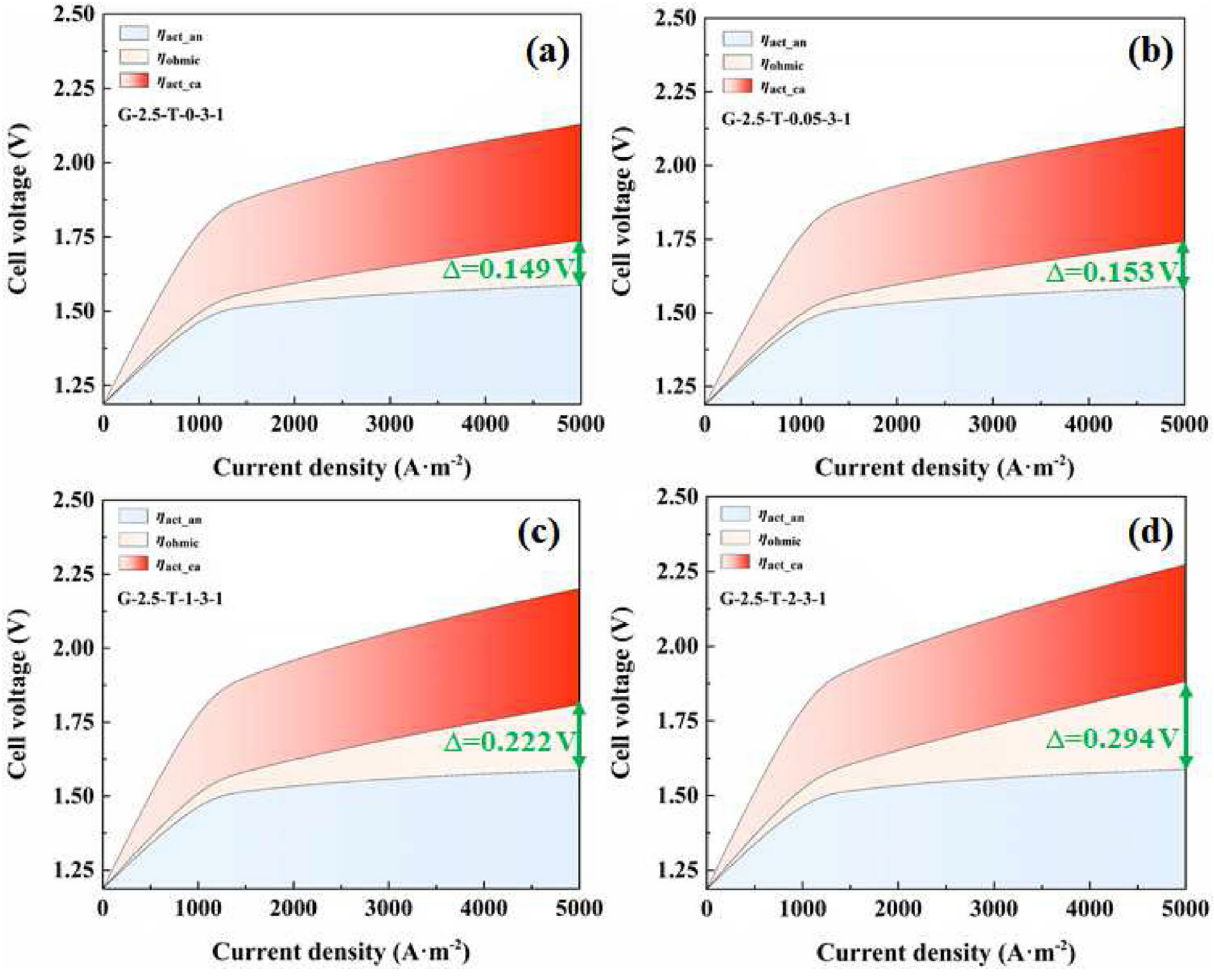

Fig. 8. Contributions of overpotential from each part of the electrolyzer with different gaps (a) G-2.5-T-0-3-1; (b) G-2.5-T-0.05-3-1; (c) G-2.5-T—1-3-1; (d) G-2.5-T—2-3-1.

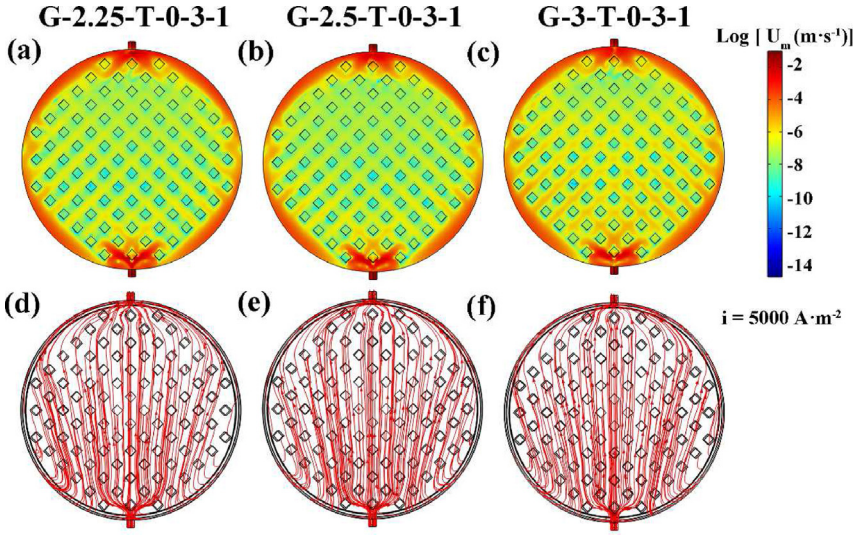

Fig. 9. Comparison in the distributions of (a—c) mixture velocity and (d—f) H_2 streamline under different channel heights.

(the number of cycles of KOH aqueous solution in the electrolyzer in 1 min) is 3.0—4.5.

Fig. 7(a—d) compares the distribution of H_2 at different flow rates (Q_{in} = 7.5, 19, 30, 45 mL·min^{-1}) inside the electrolyzer. The flow rate determines the residence time and reaction time of the material. Therefore, as the flow rate Q_{in} increases, the gas accumulated at the top of the electrode decreases, corresponding to the increase of the current density in Fig. 7(e and f). Therefore, the increase in Q_{in} is conducive to the timely removal of the gas. But when the flow rate Q_{in} was increased to 30 mL·min^{-1}, the gas reduction slowed down. This also explains the slow trend of voltage reduction in Fig. 6(b) as Q_{in} was increased to 30 mL·min^{-1}. Therefore, it is very important to select the appropriate flow rate considering the operating cost and inlet circulation. And there is an urgent need to find a flow channel structure that can quickly remove the gas in the electrolytic cell.

3.3. Influences of structural parameters on electrolyzer performance

3.3.1. Effect of the gap between the electrode and electrolyte membrane

Fig. 8 shows the distributions of ohmic overpotential and activation overpotential for electrolyzers with different gaps (h_w = 0, 0.05, 1 and 2 mm). As the gap h_w increases, the ohmic overpotential η_{ohmic} increases from 0.149 V initially to 0.294 V (green numbers of Fig. 8); and η_{act_an} is always greater than η_{act_ca}, which is due to the relatively large activation energy required for the oxidation reaction on the anode side. The ohmic overpotential between the electrode and the electrolyte membrane is also greatly affected by the bubble effect due to the increased gap. Therefore, the zero-gap electrolyzer is beneficial to improve the performance of the electrolytic cell and reduce the ohmic overpotential.

3.3.2. Effect of channel height

Fig. 9 shows the mixture velocity and H_2 streamline distributions when the channel height

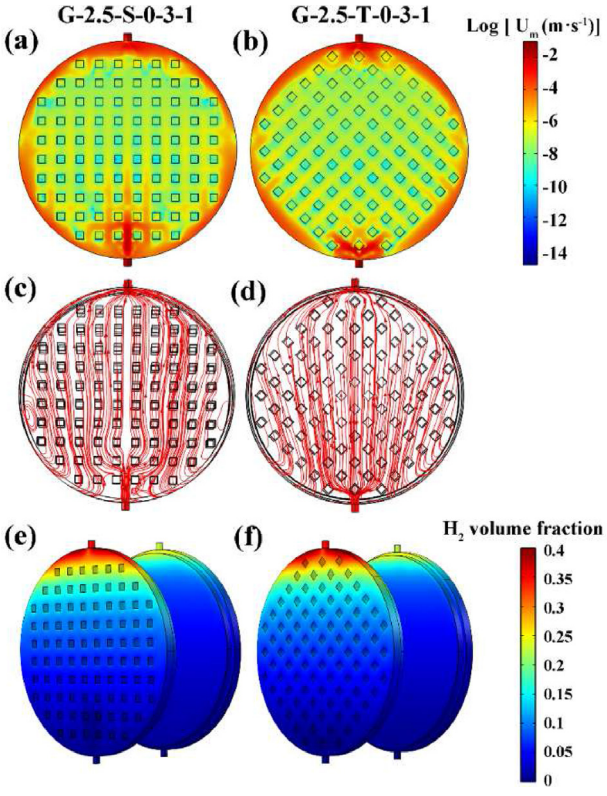

Fig. 10. Comparison in arrangements of conductive columns: (a—b) on mixture velocity; (c—d) on H_2 streamline; (e—f) on H_2 volume fraction.

h_ch values are 2.25, 2.5 and 3 mm. As shown in Fig. 9(a−c), the flow velocity distribution of the mixture is more uniform when h_ch = 3 mm. According to Fig. 9(d−f), streamlines are not significantly different. However, as shown in Fig. 9(c), due to the deepening of the flow channel, it is beneficial to buffer the change of the inlet flow rate, so the distribution of the KOH aqueous solution is more uniform, while the voltage change brought by the channel depth is not obvious.

3.3.3. Effect of arrangement of conductive columns

Based on the consistency of current density, KOH aqueous solution inlet flow rate, and electrode area between different arrangements of conductive columns circular electrolyzer, cell voltage and flow state are mainly studied.

Fig. 10(a and b) and (c−d) show the distributions of mixture flow velocity and H_2 streamline. There is a large flow velocity at the entrance and exit. The mixture flow velocity in the electrolyzer G-2.5-T-0-3-1 is larger and the distribution is more uniform, especially in the transverse direction compared with the other structure. The triangular channels increase the diffusion time, enhance the convection effect of the fluid, and further promote the discharge of gas with the electrolyte.

3.3.4. Effect of multiple outlets and inlets

From the analysis of the structure of the above electrolyzers, a single inlet and outlet will bring about the problems of inlet circulation and uneven fluid distribution. Therefore, this study designs and simulates multiple outlets and inlets electrolyzer, and compares the performance of the multiport electrolyzer with triple total flow.

Fig. 11 compares the mixture flow rates, H_2 streamlines, and volume fraction distributions for single and multiple outlets and inlets electrolyzers. Fig. 11(d and e) indicates that the H_2 streamline distribution in the electrolyzer with multiple outlets and inlets is more uniform. And the flow of the mixture in the center of the channel is significantly increased compared to a single inlet and outlet.

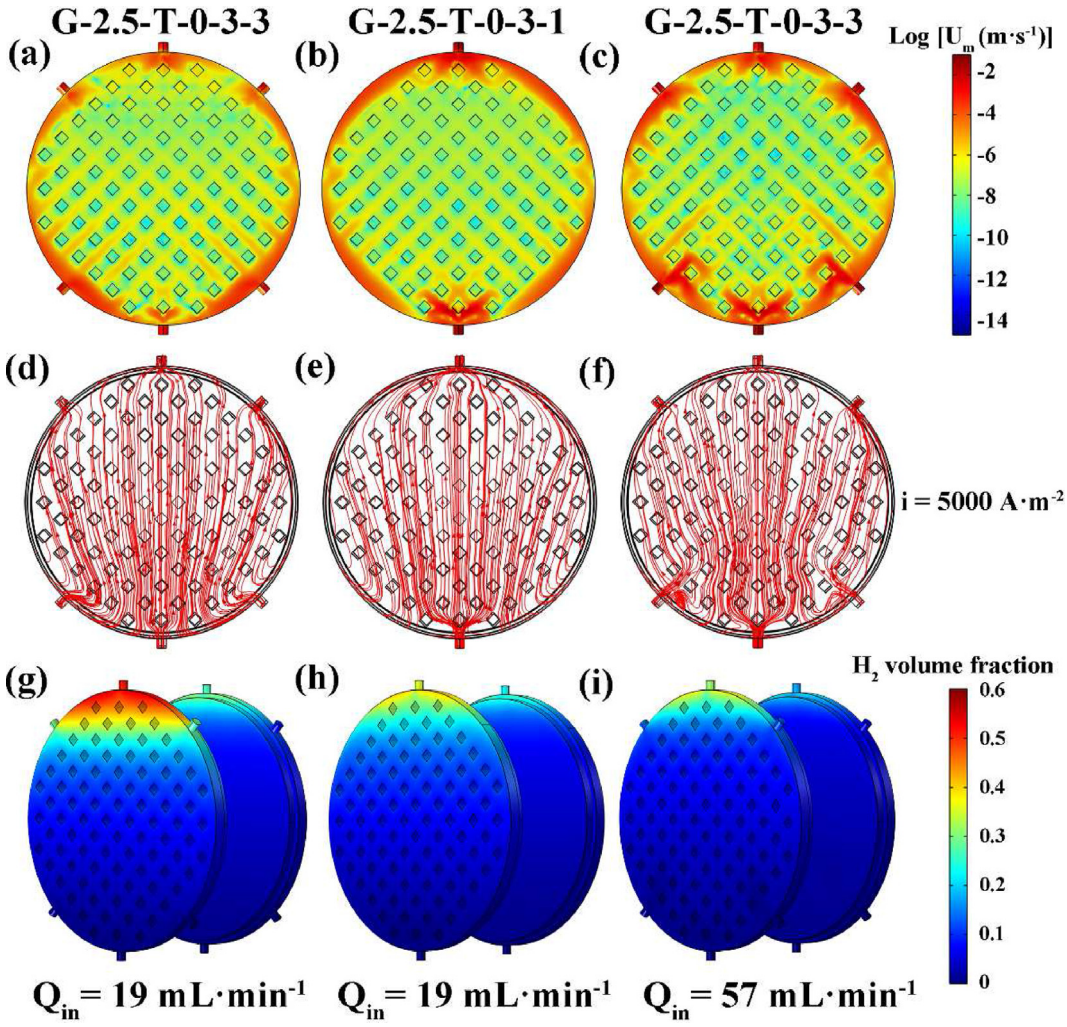

Fig. 11. Influences of the number of inlets and outlets: (a−c) on mixture velocity; (d−f) on H_2 streamline; (g−i) on H_2 volume fraction.

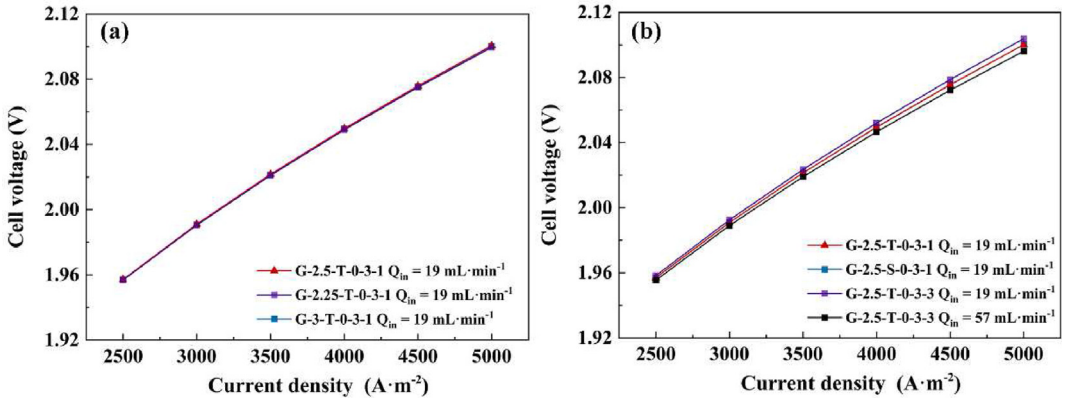

Fig. 12. Effects of different structures on cell voltage: (a) channel height; (b) channel conductive columns and inlets and outlets.

However, it is found in Fig. 11(a and b) that if only the total flow rate into the ce-ll is guaranteed to be the same, the flow rate of the mixture in the center of the channel will be very low, which is not conducive to gas removal. It suggests that increasing the flow rate appropriately is necessary for timely removal of gases, mitigation of the effects of gases on electrical conductivity, and cross-flow across the membrane using the design with multiple outlets and inlets. Multiple inlets can make the large flow more evenly distributed inside the electrolyzer.

Fig. 12(a and b) shows that the channel height and arrangement of conductive columns have little effect on the electrolysis voltage under constant current density and flow rate. While Fig. 10 suggests that the circular electrolyzer with triangular channels as shown in the electrolyzer G-2.5-T-0-3-1 is beneficial to improve the mass transfer effect. Although the multiple outlets and inlets can make the distribution of the electrolyte solution more uniform, it is still necessary to increase the electrolyte flow rate to accelerate the escape of gas, thereby reducing the retention. The voltage of the multiple outlets and inlets electrolyzer with $Q_{in} = 57\ mL \cdot min^{-1}$ is 7 mV lower than that with $Q_{in} = 19\ mL \cdot min^{-1}$ as shown in Fig. 12(b). This is

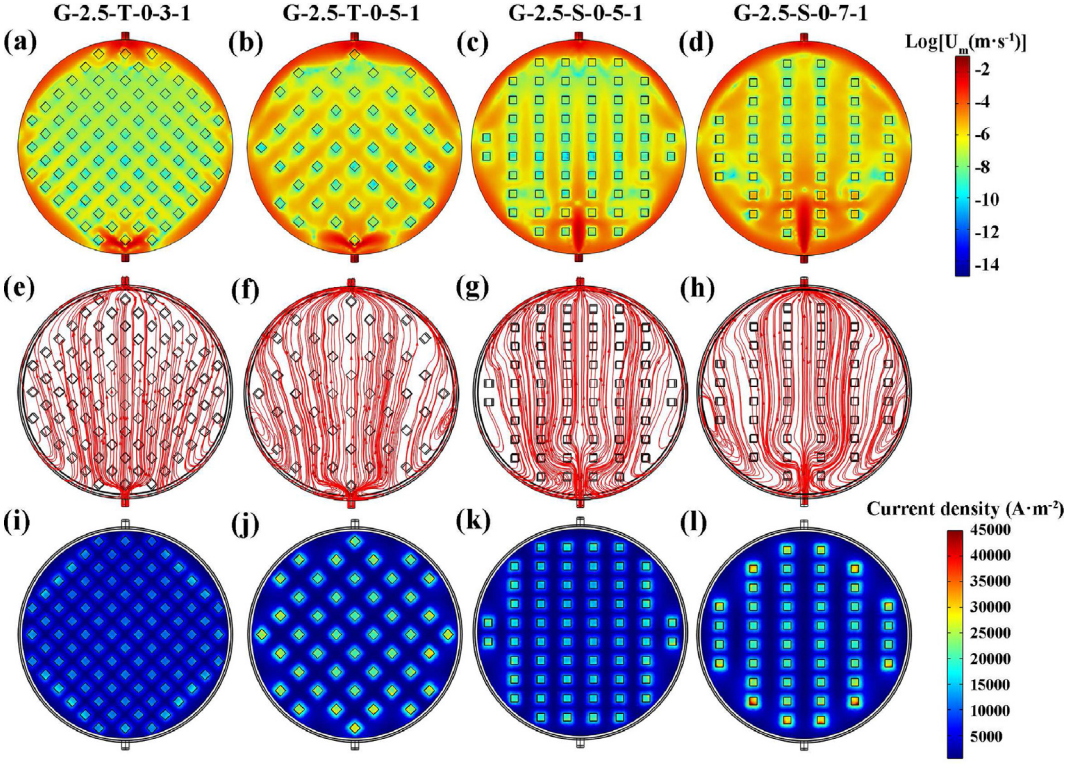

Fig. 13. Influences of spacing between conductive columns: (a—d) on mixture velocity; (e—h) on H_2 streamline; (i—l) on electrode current density.

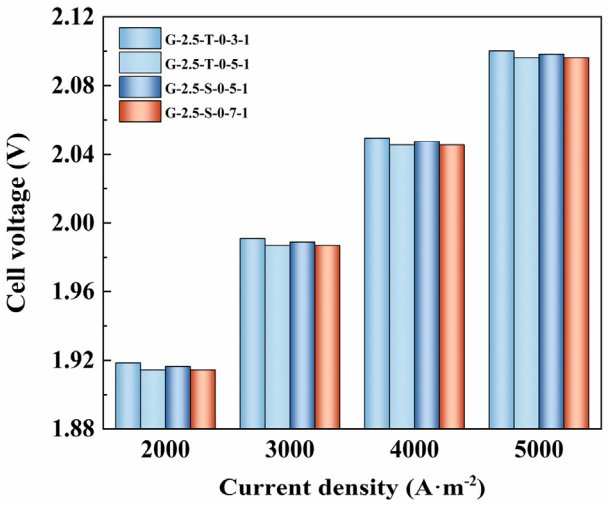

Fig. 14. Effect of spacing between conductive columns on cell voltage.

because the electrolyzer is still a small industrial electrolyzer model, so the changes brought about by these structures are not obvious. In future studies, we will continue with larger industrial electrolyzers to consider their flow field and electric field properties.

3.3.5. Effect of spacing between conductive columns

Electrolyzers G-2.5-T-0-5-1, G-2.5-S-0-5-1 and G-2.5-S-0-7-1 were constructed. As shown in Fig. 13, increasing the horizontal and vertical spacings between conductive columns of the electrolyzer can result in lower obstruction to the fluid, whereas higher center flow rate of the mixture. However, the distribution of the fluid at small spacing is also more uniform and does not cause local eddy currents as shown in Fig. 13(f—h). The number of conductive columns decreases as the

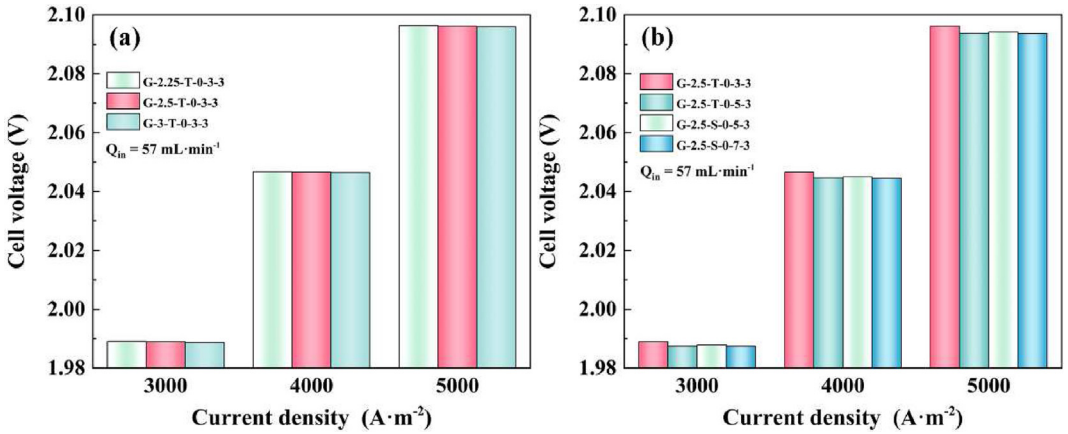

Fig. 15. The effects of (a) channel height; (b) spacing between conductive columns on cell voltage of multiple outlets and inlets electrolyzers.

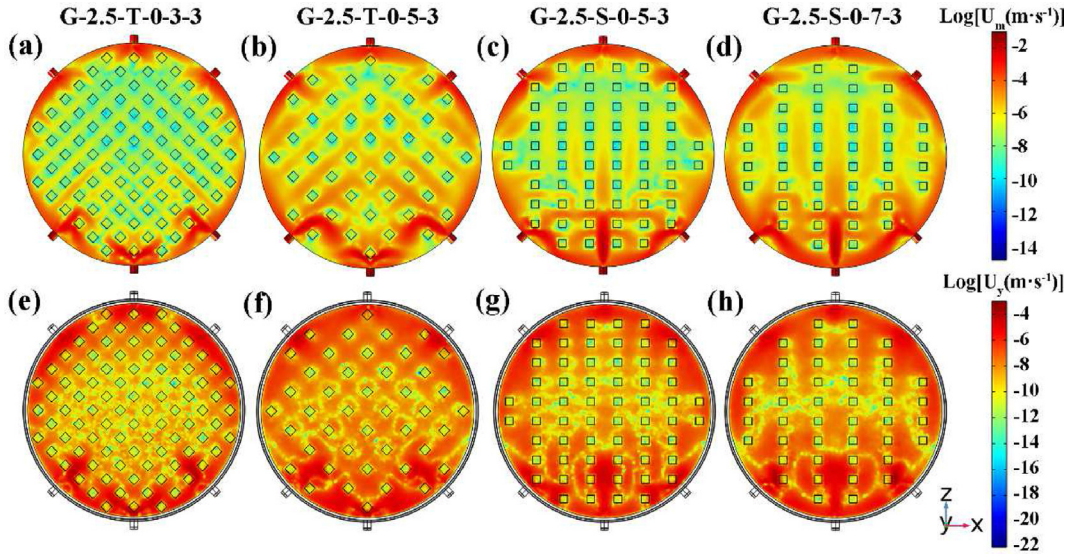

Fig. 16. Comparison in the distributions of (a—d) mixture velocity and (e—h) normal velocity of electrode surface under different spacings between conductive columns.

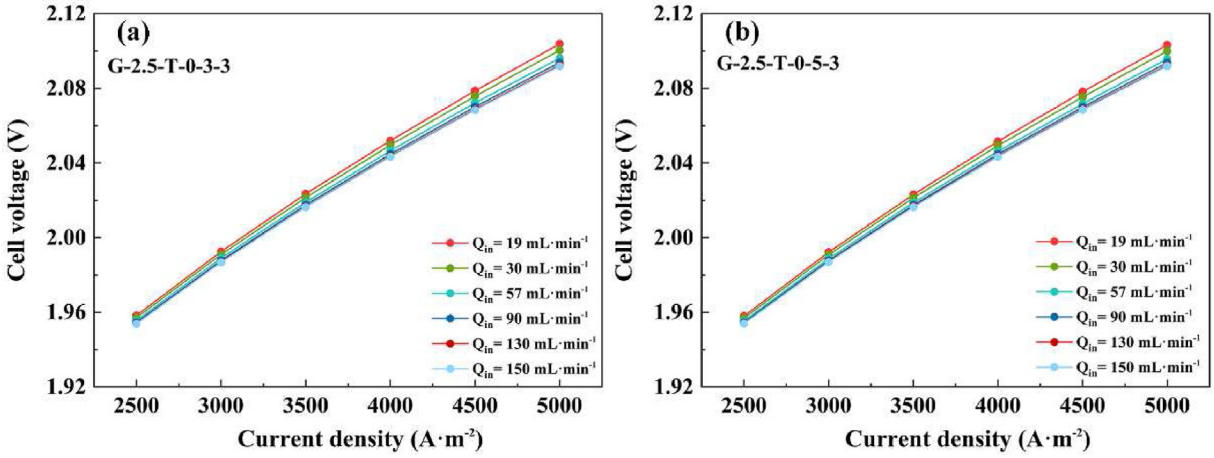

Fig. 17. The effect of Q_{in} on cell voltage of multiple outlets and inlets electrolyzers (a) G-2.5-T-0-3-3; (b) G-2.5-T-0-5-3.

width increases, so the electrode current density distribution increases in each conductive column, as reflected by Fig. 13(j–l).

Due to the increase in spacing between conductive columns, the contact area between the electrodes and channel is reduced, so the contact resistance decreases. The cell voltage with larger spacing were lower than that with the small one, with a reduction of 2–3 mV at $i = 5000$ A·m^{-2}. This shows that appropriately increasing the distance between the conductive columns is beneficial to slightly reduce the cell voltage (see Fig. 14).

3.3.6. Effect of channel height and columns spacing with multiple outlets and inlets electrolyzers

As shown in Fig. 15, the channel height has little effect on the multiple inlets and outlets electrolyzers. While increasing the spacing of the conductive columns can slightly reduce the cell voltage of multiple inlets and outlets electrolyzers.

Wide spacing of the conductive columns provides sufficient residence time for the electrolyte to enter the electrode. Fig. 16 indicates that in the multiple outlets and inlets electrolyzers, increasing the spacing of conductive columns can significantly enhance the central flow rate of KOH aqueous solution in the channel and normal flow rate of the electrode surface, thereby reducing the gas stagnation. And the electrolyzer G-2.5-T-0-5-3 performs best.

Fig. 17 illustrates that the spacings between conductive columns have a weak effect on the optimum flow range for multiple outlets and inlets electrolyzers, with the optimum flow range being 90–130 mL·min^{-1}.

4. Conclusions

Three-dimensional model coupled with the Euler-Eulerian k-ϵ turbulence and electric field reported in this paper reveals the interaction mechanism of multiphase flow state and electrochemical process inside an alkaline electrolyzer. And the influences of operating parameters and flow channel structures on the performance of the electrolyzer are studied, and the following conclusions can be made:

Increasing the concentration and flow rate Q_{in} of KOH aqueous solution facilitates to reduce the cell voltage. The cell voltage of $Q_{in} = 45.0$ mL·min^{-1} was lower than that of $Q_{in} = 7.5$ mL·min^{-1}, while when Q_{in} was higher than 30.0 mL·min^{-1}, the trend of voltage reduction slowed down. Considering the ion mass transfer and energy consumption cost, the optimum concentration and flow rate of KOH aqueous solution were 6.0–8.0 mol·L^{-1} and 30.0–45.0 mL·min^{-1}, respectively.

The zero-gap electrolyzer reduced the voltage mainly by reducing the ohmic overpotential. Triangular arrangement of conductive columns and the increase of the channel height achieved a more uniform fluid distribution, while have little effect on the voltage. And increasing the spacing between the conductive columns facilitated a lower voltage.

Multiple outlets and inlets electrolyzers with high flow rate performed the best to discharge the gas. The cell voltage with $Q_{in} = 57.0$ mL·min^{-1} was lower than that with $Q_{in} = 19.0$ mL·min^{-1}.

The electrolyzer G-2.5-T-0-5-3 contributed the best performance on reducing the cell voltage and enhancing the normal flow rate of the electrolyte on the electrode surface.

This work provides useful guidance for the optimal design of the electrolyzer structure. In future studies, models of the zero-gap electrolyzers should take into account the effects of multiphase flow within porous electrodes to predict the performance of electrolyzers more accurately.

Acknowledgments

The authors thank the National Key R&D Program (No. 2021YFB4000303) for funding and the Haihe Laboratory of Sustainable Chemical Transformations for financial support.

References

[1] Chi J, Yu H M. Water electrolysis based on renewable energy for hydrogen production[J]. Chin. J. Catal., 2018, 39(3): 390−394.
[2] Zakaria Z, Kamarudin S K. A review of alkaline solid polymer membrane in the application of aem electrolyzer: materials and characterization[J]. Int. J. Energy Res., 2021, 45(13): 18337−18354.
[3] Dong Z Y, Yang J, Yu L, Daiyan R, Amal R. A green hydrogen credit framework for international green hydrogen trading towards a carbon neutral future[J]. Int. J. Hydrogen Energy, 2022, 47(2): 728−734.
[4] Zeng K, Zhang D K. Recent progress in alkaline water electrolysis for hydrogen production and applications[J]. Prog. Energy Combust. Sci., 2010, 36(3): 307−326.
[5] Jang D, Cho H S, Kang S. Numerical modeling and analysis of the effect of pressure on the performance of an alkaline water electrolysis system[J]. Appl. Energy, 2021, 287: 116554.
[6] De Dominici G, Gabriel B. Analytical study of over-voltages in alkaline electrolysis and their parametric dependencies through a multi-physical model[J]. Int. J. Energy Res., 2021, 46(3): 3295−3323.
[7] Zhang Z Q, Xing X H. Simulation and experiment of heat and mass transfer in a proton exchange membrane electrolysis cell[J]. Int. J. Hydrogen Energy, 2020, 45(39): 20184−20193.
[8] Toghyani S, Fakhradini S, Afshari E, Baniasadi E, Abdollahzadeh Jamalabadi M Y, Safdari Shadloo M. Optimization of operating parameters of a polymer exchange membrane electrolyzer[J]. Int. J. Hydrogen Energy, 2019, 44(13): 6403−6414.
[9] Lee C H, Lee J K, Zhao B, Fahy K F, LaManna J M, Baltic E, Hussey D S, Jacobson D L, Schulz V P, Bazylak A. Temperature-dependent gas accumulation in polymer electrolyte membrane electrolyzer porous transport layers[J]. J. Power Sources, 2020, 446: 227312.
[10] Jang D, Choi W, Cho H S, Cho W C, Kim C H, Kang S. Numerical modeling and analysis of the temperature effect on the performance of an alkaline water electrolysis system[J]. J. Power Sources, 2021, 506: 230106.
[11] Han B, Steen S M, Mo J, Zhang F Y. Electrochemical performance modeling of a proton exchange membrane electrolyzer cell for hydrogen energy[J]. Int. J. Hydrogen Energy, 2015, 40(22): 7006−7016.
[12] Abdin Z, Webb C J, Gray E M. Modelling and simulation of an alkaline electrolyser cell[J]. Energy, 2017, 138: 316−331.
[13] Alexiadis A, Dudukovic M P, Ramachandran P, Cornell A, Wanngård J, Bokkers A. Liquid-gas flow patterns in a narrow electrochemical channel[J]. Chem Eng Sci, 2011, 66(10): 2252−2260.
[14] De Groot M T, Vreman A W. Ohmic resistance in zero gap alkaline electrolysis with a zirfon diaphragm[J]. Electrochim. Acta, 2021, 369: 137684.
[15] Rodríguez J, Amores E. CFD modeling and experimental validation of an alkaline water electrolysis cell for hydrogen production[J]. Processes, 2020, 8(12): 1634.
[16] Vogt H, Balzer R J. The bubble coverage of gas-evolving electrodes in stagnant electrolytes[J]. Electrochim. Acta, 2005, 50(10): 2073−2079.
[17] Li Y, Kang Z, Mo J, Yang G, Yu S, Talley D A, Han B, Zhang F Y. *In-situ* investigation of bubble dynamics and two-phase flow in proton exchange membrane electrolyzer cells[J]. Int. J. Hydrogen Energy, 2018, 43(24): 11223−11233.
[18] Wong X Y, Zhuo Y T, Shen Y S. Numerical analysis of hydrogen bubble behavior in a zero-gap alkaline water electrolyzer flow channel[J]. Ind. Eng. Chem. Res., 2021, 60(33): 12429−12446.
[19] Lee J, Alam A, Park C, Yoon S, Ju H. Modeling of gas evolution processes in porous electrodes of zero-gap alkaline water electrolysis cells[J]. Fuel, 2022, 315: 123273.
[20] Boissonneau P, Byrne B P. An experimental investigation of bubble-induced free convection in a small electrochemical cell[J]. J. Appl. Electrochem., 2000, 30(7): 767−775.
[21] Aldas K, Pehlivanoglu N, Mat M D. Numerical and experimental investigation of two-phase flow in an electrochemical cell[J]. Int. J. Hydrogen Energy, 2008, 33(14): 3668−3675.
[22] Phillips R, Edwards A, Rome B, Jones D R, Dunnill C W. Minimising the ohmic resistance of an alkaline electrolysis cell through effective cell design[J]. Int. J. Hydrogen Energy, 2017, 42(38): 23986−23994.
[23] Haverkort J W, Rajaei H. Voltage losses in zero-gap alkaline water electrolysis[J]. J. Power Sources, 2021, 497: 229864.
[24] Bratsch S G. Standard electrode potentials and temperature coefficients in water at 298.15 k[J]. J. Phys. Chem. Ref. Data, 1989, 18(1): 1−21.
[25] Gilliam R, Graydon J, Kirk D, Thorpe S. A review of specific conductivities of potassium hydroxide solutions for various concentrations and temperatures[J]. Int. J. Hydrogen Energy, 2007, 32(3): 359−364.
[26] González-Buch C, Herraiz-Cardona I, Ortega E, García-Antón J, Pérez-Herranz V. Synthesis and characterization of macroporous Ni, Co and Ni-Co electrocatalytic deposits for hydrogen evolution reaction in alkaline media[J]. Int. J. Hydrogen Energy, 2013, 38(25): 10157−10169.
[27] Mrjdha M SH, Kibria M F. Electrochemical studies of the nickel electrode for the oxygen evolution reaction[J]. Int. J. Hydrogen Energy, 1996, 21: 179−182.
[28] Torii K, Kodama M, Hirai S. Three-dimensional coupling numerical simulation of two-phase flow and electrochemical phenomena in alkaline water electrolysis[J]. Int. J. Hydrogen Energy, 2021, 46(71): 35088−35101.
[29] Weijs M, Janssen L JJ J, Visser G. Ohmic resistance of solution in a vertical gas-evolving cell[J]. J. Appl. Electrochem., 1997, 27(4): 371−378.
[30] Zarghami A, Deen N G, Vreman A W. CFD modeling of multiphase flow in an alkaline water electrolyzer[J]. Chem. Eng. Sci., 2020, 227: 115926.
[31] Behbahani R M. Chemical engineering module: comsol user's guide[M]. 2013.
[32] Amores Vera E, Rodríguez Ruiz J, Merino Rodríguez C, García Escribano P. Study of an alkaline electrolyzer powered by renewable energy[C]//Proceedings of the COMSOL Conference, 26−28 October 2011. Stuttgart, Germany.
[33] Magnussen O M, Gross A. Toward an atomic-scale understanding of electrochemical interface structure and dynamics[J]. J. Am. Chem. Soc., 2019, 141(12): 4777−4790.
[34] Karacan C, Lohmann-Richters F P, Keeley G P, Scheepers F, Shviro M, Müller M, Carmo M, Stolten D. Challenges and important considerations when benchmarking single-cell alkaline electrolyzers[J]. Int. J. Hydrogen Energy, 2022, 47(7): 4294−4303.

碱性电解槽三维两相 CFD 模拟研究

高玲玉 [a]，杨琳 [a]，王晨辉 [a]，单桂轩 [a]，霍欣怡 [a]，张梦飞 [a]，李韡 [a,b]，张金利 [a,b,*]
[a] 天津大学化工学院，天津 300072
[b] 物质绿色创造与制造海河实验室，天津 300192

摘要

电解槽的结构和运行参数对碱性水电解的性能起着重要作用。针对工业碱性水电解槽紧凑的装配结构，特别是在电流密度大于 5000 $A \cdot m^{-2}$ 时，本文首次建立了耦合电场和欧拉-欧拉 k-ε 湍流流场的三维数值模型，以准确模拟碱性水电解槽的性能。将模拟结果与实验数据进行比较，验证了模型的准确性。通过电解槽内部电场和流场特性的反馈，确定了适合的浓度、流量的操作条件和流道结构的优化设计方法。适当增加电解液浓度和流速有利于降低槽电压。KOH 水溶液的最佳浓度和流速分别为 6.0 – 8.0 $mol \cdot L^{-1}$ 和 30.0 – 45.0 $mL \cdot min^{-1}$。随着电极与隔膜距离的增加，欧姆过电压显著增加；流道高度和双极板上导流柱的排列方式对电压的影响微弱，但三角形排列的导流柱和流道高度的增加有利于提高流体的分布均匀度，适当增加导流柱之间的距离有利于降低槽电压。多流体出入口电解槽有利于产生更均匀的流体分布，流道高度对多出入口电解槽同样影响不大。宽导流柱间距的多流体出入口电解槽 G-2.5-T-0-5-3，配合高流量，既能降低槽电压，又能提高电解质在电极面的法向流速，使电解槽发挥最佳性能。本工作对碱性水电解高效电解槽的放大设计和优化具有一定指导意义。

关键词：碱性电解槽；三维；两相流；流道；电流密度分布